Three-dimensional coherence imaging in the Fresnel domain

Daniel L. Marks, Ronald A. Stack, and David J. Brady

We show that three-dimensional incoherent primary sources can be reconstructed from finite-aperture Fresnel-zone mutual intensity measurements by means of coordinate and Fourier transformation. The spatial bandpass and impulse response for three-dimensional imaging that result from use of this approach are derived. The transverse and longitudinal resolutions are evaluated as functions of aperture size and source distance. The longitudinal resolution of three-dimensional coherence imaging falls inversely with the square of the source distance in both the Fresnel and Fraunhofer zones. We experimentally measure the three-dimensional point-spread function by using a rotational shear interferometer. © 1999 Optical Society of America

OCIS codes: 030.1640, 110.1650, 110.4850, 100.3010, 100.6890, 070.4550.

1. Introduction

Improvements in electronic sensors, automated positioning systems, and data processing equipment render optical coherence imaging of complex three-dimensional (3D) objects increasingly practical. Two-dimensional (2D) imaging based on the far-field van Cittert–Zernike theorem has been used in radio astronomy for more than two decades.[1] Recently, coherence imaging techniques have begun to shift back to the optical domain,[2,3] and a number of optical systems have been implemented or are under development.[4]

Several researchers have generalized the van Cittert–Zernike theorem to 3D source distributions and have shown that 3D inversion is possible in the far field.[5,6] LaHaie[7] describes modal 3D reconstruction techniques that also work in the near and Fresnel zones. Zarubin notes that the 3D generalized van Cittert–Zernike theorem applies in the Fresnel zone under certain coherence assumptions and that the theorem can also be applied to x-ray and particle scattering.[8] More recently, 3D source re- construction from a finite far-field aperture by use of the generalized 3D theorem was analyzed and experimentally demonstrated.[9–11] Unlike pseudo-3D techniques such as holography and stereo imaging, coherence imaging provides a true 3D model of object sources.

In this paper we show that Fourier reconstruction techniques can be applied to Fresnel-zone reconstruction by application of a coordinate transformation to the generalized van Cittert–Zernike theorem. This extension is important because the object distance may be much less for a given aperture and wavelength in the Fresnel zone than in the Fraunhofer zone. Because longitudinal resolution falls as the square of object distance, longitudinal resolution in the Fresnel zone may exceed longitudinal resolution in the Fraunhofer zone by several orders of magnitude.

In Section 2 of this paper we review the Fourier-transform relationship between the source intensity distribution and the far-field mutual intensity and describe the coordinate transformation by which a similar relationship is obtained between the source distribution and the Fresnel-zone mutual intensity. In Section 3 we explore the bandpass and resolution limits of 3D coherence imaging. Resolution constraints are easily visualized by use of the 3D spatial bandpass, or band volume, because in limited-aperture systems the band volume has precise boundaries.[12,13] The resolution along any given direction is inversely proportional to the extent of the band volume along that direction. In Section 3 we analyze the band volume and the impulse response for two particular coherence measurement systems,

The authors are with the Beckman Institute for Advanced Science and Technology and Department of Electrical and Computer Engineering, University of Illinois at Urbana—Champaign, Urbana, Illinois 61801. D. J. Brady's e-mail address is dbrady@uiuc.edu.
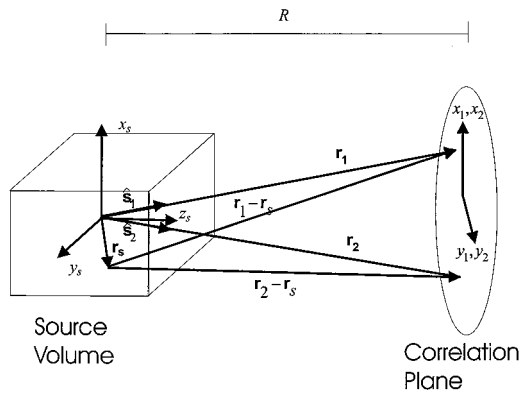
Fig. 1. Measurement geometry for coherence imaging. An incoherent primary source distribution in the source volume is imaged by use of two-point correlation measurements drawn from the correlation plane. The separation between the volumes is greater than the extent of either volume. The correlation point coordinates are (x_1, y_1) for the first point and (x_2, y_2) for the second point. The correlation points are scanned throughout the correlation plane to yield the mutual intensity. $\mathbf{r}_1$, $\mathbf{r}_2$, vectors from the source volume origin to (x_1, y_1) and (x_2, y_2); $\hat{s}_1$, $\hat{s}_2$, unit vectors parallel to $\mathbf{r}_1$ and $\mathbf{r}_2$; $\mathbf{r}_s$, position vector in the source volume.

the Michelson stellar interferometer and the rotational shear interferometer. In Section 4 we show experimental reconstructions obtained from an implementation of the rotational shear interferometer.

2. Fourier Inversion of the Generalized Van Cittert–Zernike Theorem

The mutual intensity for a quasi-monochromatic 3D incoherent primary source can be expressed in terms of the source radiant power density by use of the Hopkins integral:

$$J(\mathbf{r}_1, \mathbf{r}_2) = \left(\frac{k_0}{2\pi}\right)^2 \int_\sigma I(\mathbf{r}_s)$$

$$\times \frac{\exp[jk_0(|\mathbf{r}_1 - \mathbf{r}_s| - |\mathbf{r}_2 - \mathbf{r}_s|)]}{|\mathbf{r}_1 - \mathbf{r}_s||\mathbf{r}_2 - \mathbf{r}_s|}\, d^3\mathbf{r}_s, \quad (1)$$

where σ is the source volume, $I(\mathbf{r}_s)$ is the 3D source radiant power density, $J(\mathbf{r}_1, \mathbf{r}_2)$ is the mutual intensity at field sample positions $\mathbf{r}_1$ and $\mathbf{r}_2$, and $k_0 = 2\pi/\lambda_0$ is the wave number of the optical field at wavelength λ_0.[14] The geometry of the radiation and measurement space is illustrated in Fig. 1. $\mathbf{r}_s$ is the position vector in the source volume. $J(\mathbf{r}_1, \mathbf{r}_2)$ is measured between pairs of points drawn from an aperture labeled the correlation plane. The correlation plane lies a distance R along the z axis from the center of the correlation volume. As is shown in the figure, $\mathbf{r}_1$ and $\mathbf{r}_2$ are vectors from the origin of the source volume to field sampling points on the correlation plane. $J(\mathbf{r}_1, \mathbf{r}_2)$ is the zero-delay mutual coherence function between the field at $\mathbf{r}_1$ and that at $\mathbf{r}_2$. Systems for measuring $J(\mathbf{r}_1, \mathbf{r}_2)$ are described in section 3.

The goal of coherence imaging is to invert Eq. (1) and reconstruct $I(\mathbf{r}_s)$ from measurements of $J(\mathbf{r}_1, \mathbf{r}_2)$.

Inversion was previously shown to be straightforward in the Fraunhofer zone, where Eq. (1) reduces to the generalized van Cittert–Zernike theorem

$$J(r_1\hat{s}_1, r_2\hat{s}_2) = \tilde{I}\left[\frac{(\hat{s}_1 - \hat{s}_2)}{\lambda_0}\right]\frac{\exp[jk_0(r_1 - r_2)]}{\lambda_0^2 r_1 r_2}, \quad (2)$$

where $\hat{s}_1$ and $\hat{s}_2$ are unit vectors in the $\mathbf{r}_1$ and $\mathbf{r}_2$ directions, $r_1 = |\mathbf{r}_1|$, $r_2 = |\mathbf{r}_2|$, and $\tilde{I}(\mathbf{u})$ is the 3D Fourier transform of the source intensity distribution.[5,6] $\mathbf{u}$ is the position vector of $I(\mathbf{r}_s)$ in 3D Fourier space. According to Eq. (2), measurement of $J(\mathbf{r}_1, \mathbf{r}_2)$ over a range in $\mathbf{r}_1 = r_1\hat{s}_1$ and $\mathbf{r}_2 = r_2\hat{s}_2$ yields samples of $\tilde{I}(\mathbf{u})$ for $\mathbf{u}$ over the range $(\hat{s}_1 - \hat{s}_2)/\lambda_0$. Inasmuch as variations in r_1 and r_2 do not affect the range sampled in $\mathbf{u}$, it is sufficient to measure $J(\mathbf{r}_1, \mathbf{r}_2)$ for $\mathbf{r}_1$ and $\mathbf{r}_2$ drawn from a surface surrounding the object rather than a volume. Doing so reduces the six-dimensional measurement space of $J(\mathbf{r}_1, \mathbf{r}_2)$ to four dimensions. Even for $\mathbf{r}_1$ and $\mathbf{r}_2$ drawn from a surface, redundant values of $(\hat{s}_1 - \hat{s}_2)/\lambda_0$ will be obtained. To characterize $I(\mathbf{r}_s)$ to wavelength-limited resolution it is necessary only to sample $J(\mathbf{r}_1, \mathbf{r}_2)$ over a 3D subspace of $\mathbf{r}_1 \otimes \mathbf{r}_2$ that fully samples the range of $\hat{s}_1 - \hat{s}_2$. If $J(\mathbf{r}_1, \mathbf{r}_2)$ is measured over this subspace, $\tilde{I}(\mathbf{u})$ is known for all $\mathbf{u}$ such that $|\mathbf{u}| \leq 2/\lambda_0$. The sphere $|\mathbf{u}| \leq 2/\lambda_0$ is the band volume for this imaging system. The band volume is the 3D spatial bandpass of the imaging system. The impulse response of the system is the inverse Fourier transform of the band volume. For the fully sampled imaging system, the impulse response will be spherically symmetric, with a resolution of approximately $\lambda_0/2$.

In most optical imaging situations, particularly the far-field systems to which Eq. (2) applies, the source volume is remote from the correlation space. In such cases it is not possible to measure $J(\mathbf{r}_1, \mathbf{r}_2)$ over a surface that encloses the source. Rather, the goal for these systems is to reconstruct $I(\mathbf{r}_s)$ from measurements of $J(\mathbf{r}_1, \mathbf{r}_2)$ over a limited range of $\hat{s}_1$ and $\hat{s}_2$. The limited range is illustrated in Fig. 1 by the circular aperture in the correlation plane. The effect of limiting the range of $\hat{s}_1$ and $\hat{s}_2$ is to limit further the range of $\mathbf{u}$ and thereby to reduce the band volume and the imaging resolution.

Rosen and Yariv previously considered source reconstruction from a finite aperture in the far field.[9–11] The result of Rosen and Yariv is obtained by expansion of $\hat{s}_1$ and $\hat{s}_2$ in terms of the planar coordinates of the correlation plane as, for example,

$$\hat{s}_1 \approx \frac{x_1}{R}\hat{\mathbf{i}}_x + \frac{y_1}{R}\hat{\mathbf{i}}_y + \left(1 - \frac{x_1^2 + y_1^2}{2R^2}\right)\hat{\mathbf{i}}_z, \quad (3)$$

where R is the distance from the origin of the source volume to the sampling plane. The range over which $\tilde{I}(\mathbf{u})$ is determined from measurements of $J(R\hat{s}_1, R\hat{s}_2)$ in this plane is

$$\mathbf{u} = \frac{(\hat{s}_1 - \hat{s}_2)}{\lambda_0} \approx \frac{\Delta x}{\lambda_0 R}\hat{\mathbf{i}}_x + \frac{\Delta y}{\lambda_0 R}\hat{\mathbf{i}}_y - \frac{\hat{x}\Delta x + \hat{y}\Delta y}{\lambda_0 R^2}\hat{\mathbf{i}}_z, \quad (4)$$
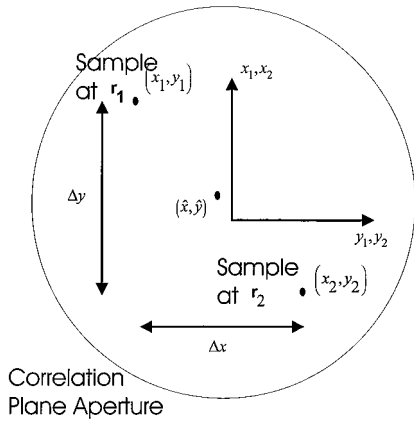
Fig. 2. Coordinate geometry in the sampling plane. Source inversion is simplified by use of the transformed coordinates $(\Delta x, \Delta y)$ $= (x_1 - x_2, y_1 - y_2)$, $(\hat{x}, \hat{y}) = [(x_1 + x_2)/2, (y_1 + y_2)/2]$, $q = \Delta x\hat{x} +$ $\Delta y\hat{y}$.

where $\hat{x} = (x_1 + x_2)/2, \hat{y} = (y_1 + y_2)/2, \Delta x = (x_1 - x_2)$, and $\Delta y = (y_1 - y_2)$. These correlation plane variables are illustrated in Fig. 2. Many different combinations of $\hat{x}, \Delta x, \hat{y}$, and Δy may result in the same $\hat{\mathbf{i}}_z$ coordinate in $\mathbf{u}$. To recover all the nonredundant information about $\tilde{I}(\mathbf{u})$ available for a given range in $(\hat{x}, \hat{y}, \Delta x, \Delta y)$ one need only measure the mutual intensity over a 3D projection of the four-dimensional $\hat{x}, \Delta x, \hat{y}$, and Δy space. The 3D projection should sample all allowed values of $\Delta x, \Delta y$, and $\hat{x}\Delta x + \hat{y}\Delta y$. As in Refs. 9–11, we define a variable $q = \hat{x}\Delta x + \hat{y}\Delta y$. We then define the new function $J_{3D}(\Delta x, \Delta y, q)$, which is $J(\mathbf{r}_1, \mathbf{r}_2)$ restricted to the $\Delta x, \Delta y, q$ subspace. In this subspace, Eq. (2) becomes

$$J_{3D}(\Delta x, \Delta y, q) = \frac{1}{\lambda_0^2 R^2} \tilde{I}\left(u_x = \frac{\Delta x}{\lambda_0 R},\right.$$
$$\left. u_y = \frac{\Delta y}{\lambda_0 R}, u_z = -\frac{q}{\lambda_0 R^2}\right). \quad (5)$$

$J_{3D}(\Delta x, \Delta y, q)$ is sampled from two-point correlations over the correlation plane of Fig. 1. The source distribution is recovered from these measurements by inverse Fourier transformation of Eq. (5), which yields

$$I(\mathbf{r}_s) * P_\rho(\mathbf{r}_s) = \lambda R^2 \iiint_\rho J_{3D}(\Delta x, \Delta y, q)$$
$$\times \exp\left(\frac{j2\pi x_s \Delta x}{\lambda_0 R} + \frac{j2\pi y_s \Delta y}{\lambda_0 R}\right.$$
$$\left. - \frac{j2\pi z_s q}{\lambda_0 R^2}\right) d\Delta x d\Delta y dq, \quad (6)$$

where ρ is the range over which the mutual intensity is measured in $(\Delta x, \Delta y, q)$ space and $P_\rho(\mathbf{r}_s)$ is an impulse response for the coherence imaging system. $P_\rho(\mathbf{r}_s)$ is the inverse Fourier transform of the band volume. The band volume in this case is proportional to the sample range in $(\Delta x, \Delta y, q)$. The anal-

ysis leading to Eq. (5) follows discussions in previous publications, especially as presented in Ref. 11.

To derive the Fresnel-zone Fourier relationship we begin again with Eq. (1). Both the Fresnel- and the far-zone approximations rely on paraxial approximations of $|\mathbf{r}_1 - \mathbf{r}_s|$ and $|\mathbf{r}_2 - \mathbf{r}_s|$. The far-field approximation of relation (3), however, includes an assumption that $1/R$ is an accurate approximation of $1/(R - z_s)$ for all points in the source volume at (x_s, y_s, z_s). This assumption severely restricts the transverse extent of the source, as discussed below. Rather than make this assumption, we substitute $1/(R - z_s)$ for $1/R$ in the paraxial approximation. The resultant equations are substantially simpler if we shift the origin of the z axis to the correlation plane. To do this, we define a new variable, $z_{sp} = R - z_s$. The correlation plane then corresponds to the $z_{sp} = 0$ plane, and the paraxial approximation is

$$|\mathbf{r}_1 - \mathbf{r}_s| \approx z_{sp} + \frac{(x_1 - x_s)^2}{2z_{sp}} + \frac{(y_1 - y_s)^2}{2z_{sp}} + \dots . \quad (7)$$

Substituting expression (7) into Eq. (1) yields

$$J(\mathbf{r}_1, \mathbf{r}_2) = \iiint_\sigma \frac{I(\mathbf{r}_{sp})}{\lambda^2 z_{sp}^2} \exp\left[-\frac{j2\pi}{\lambda_0 z_{sp}}(x_s \Delta x + y_s \Delta y)\right.$$
$$\left. + \frac{j2\pi}{\lambda_0 z_{sp}}(\hat{x}\Delta x + \hat{y}\Delta y)\right] d^3 \mathbf{r}_{sp}, \quad (8)$$

where $\mathbf{r}_{sp}$ is the position vector in the source coordinates (x_s, y_s, z_{sp}) and, as above, Δx and Δy are the separations between the sampling points and $\hat{x}$ and $\hat{y}$ are the mean positions of the sampling points on the correlation plane. We can obtain Eq. (5) from Eq. (8) if we assume that $1/z_{sp} \approx (1/R)[1 - (z_s/R)]$, such that $(z_s x_s \Delta x)/(\lambda R^2), (z_s y_s \Delta y)/(\lambda R^2) \ll 1$, and that the range of (x_s, y_s) is much less than the range of $(\hat{x}, \hat{y})$. These approximations would mean that the longitudinal extent of the source must be much less than the mean source range and that the transverse extent of the source must be much less than the mean interferometer displacement. These are relatively harsh limitations, particularly in view of the quadratic decrease in range resolution with increasing range.

We can express Eq. (8) as a Fourier transform without making these approximations if we transform the source coordinates into the projective coordinates[15]

$$x' = \frac{x_s}{z_{sp}}, \qquad y' = \frac{y_s}{z_{sp}}, \qquad z' = \frac{1}{z_{sp}} \quad (9)$$

Figure 3 illustrates the transformation between the source coordinates (x_s, y_s, z_{sp}) and the (x', y', z') coordinate system. x' and y' are equal to the tangents of the angles θ_x and θ_y between the ray from the correlation plane's origin to the source point (x_s, y_s, z_{sp}) and to the planes $y_s = 0$ and $x_s = 0$, respectively. In the small-angle approximation, $x' = \theta_x$ and $y' = \theta_y$. Figure 3 is drawn in Cartesian space and shows grids of constant x', y' in the projective space. As indicated by the distortion between the grids, uniform
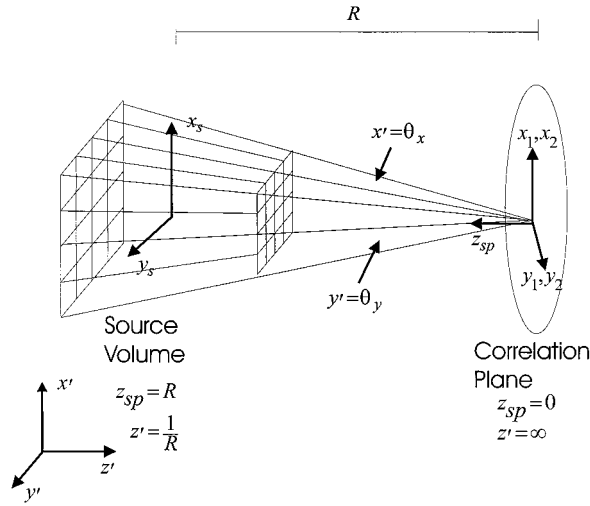
Fig. 3. Relationship between the Cartesian source coordinates and the projective coordinates. The origin of longitudinal coordinate z_{sp} is in the correlation plane. Longitudinal projective coordinate $z' = 1/z_{sp}$ has an origin at $z_{sp} = \infty$ and is equal to $1/R$ at the center of the source volume. In the small-angle approximation, the transverse projective coordinates $x' = z'x_s$ and $y' = z'y_s$ correspond to the angles θ_x and θ_y between the $y = 0$ and $x = 0$ planes and the ray from the correlation plane origin to the real-space source point.

sampling in the primed coordinate system yields nonuniform samples in Cartesian space. The orientation of the primed axes is shown at the lower left of Fig. 3. The origin of the z' axis is at $z_{sp} = \infty$ off the left of the figure. The correlation plane, which is assumed not to lie in the source volume, is at $z' = \infty$.

One can translate displacements in the (x', y', z') coordinate system into real space displacements by using the differential relationships

$$dx = \frac{z'dx' - x'dz'}{z'^2}, \qquad dy = \frac{z'dy' - y'dz'}{z'^2},$$

$$dz = -\frac{dz'}{z'^2}. \qquad (10)$$

Neglecting the dz' dependence of the x and y resolutions and substituting $z = 1/z'$ simplify these relationships to

$$dx = zdx', \qquad dy = zdy', \qquad dz = z^2dz'. \qquad (11)$$

These relationships quantify the distorted Cartesian space grid sampling shown in Fig. 3. For example, uniform steps in dz' yield grid spaces that increase as z^2 in real space. The sampling resolution decreases in both the transverse and the longitudinal directions as the distance from the image plane increases, but the angular grid spacings dx/z and dy/z remain constant.

In the primed coordinates Eq. (8) becomes

$$J_{3D}(\Delta x, \Delta y, q) = \iiint_{\sigma'} \frac{I(x', y', z')}{\lambda_0^2 z'^2}$$

$$\times \exp\left[\frac{-j2\pi}{\lambda_0}(x'\Delta x + y'\Delta y)\right.$$

$$\left. + \frac{j2\pi}{\lambda_0}z'q\right]d^3\mathbf{r'}, \qquad (12)$$

where σ' is the source volume expressed in the transformed coordinates. As in the far-field case, $q = \hat{x}\Delta x + \hat{y}\Delta y$ and $J_{3D}(\Delta x, \Delta y, q)$ is $J(\mathbf{r}_1, \mathbf{r}_2)$ in the 3D subspace. Note that the Jacobian factor for the differential (z'^{-4}) combines with the denominator of source radiation factor (z^2) to maintain the form of the $1/z'^2$ radiation factor. Equation (12) can be expressed in analogy with Eq. (5) as

$$J_{3D}(\Delta x, \Delta y, q) = \frac{1}{\lambda^2}\tilde{I}_p\left(\frac{\Delta x}{\lambda_0}, \frac{\Delta y}{\lambda_0}, \frac{q}{\lambda_0}\right), \qquad (13)$$

where $\tilde{I}_p(\mathbf{u})$ is the 3D Fourier transform with respect to (x', y', z') of $I(x', y', z')/z'^2$. Since care must be taken to avoid the singularity at $z' = 0$, the Fourier transform of $I(x', y', z')/z'^2$ cannot be taken over unbounded space. The range of integration is bounded by the assumption that the source distribution has finite support and that the correlation plane is far removed from the source. As in the far-field case, one recovers the incoherent intensity distribution of the distributed source by inverse Fourier transforming Eq. (13), using the mutual intensity sampled in the correlation plane in pairs of coordinates parameterized in $(\Delta x, \Delta y, q)$. In analogy with Eq. (6), this approach yields

$$\left[\frac{I(x', y', z')}{z'^2}\right] * P_\rho(\mathbf{r'}) = \lambda\iiint_\rho J_{3D}(\Delta x, \Delta y, q)$$

$$\times \exp\left[\frac{j2\pi}{\lambda_0}(x'\Delta x + y'\Delta y)\right.$$

$$\left. - \frac{j2\pi}{\lambda_0}z'q\right]d\Delta x d\Delta y dq. \qquad (14)$$

The source intensity in the Cartesian-space coordinate system is determined by transformation of $I(\mathbf{r'})$ to the $\mathbf{r}_s$ coordinate system. As in the far-zone case, $P_\rho(\mathbf{r'})$ is the Fourier transform of the band volume. The primary difference between Eqs. (5) and (6) and Eqs. (13) and (14) is that the ratio of the source extent to the source range can be larger in the latter. This means that Eqs. (13) and (14) can accurately reconstruct a source of a given size from a closer range than can Eqs. (5) and (6). Because the band volume in both cases scales with the ratio of lateral aperture to the source range, a closer range means a bigger band volume and better resolution.

3. Measurement Systems, Band Volume, and Impulse Response

In Section 2 we derived source-reconstruction algorithms from limited-aperture coherence measurements. In this section we consider two particular physical systems for obtaining these coherence measurements and we analyze the band volume and the impulse response for each system. The two systems that we consider are the Michelson stellar interferometer (MSI) and the rotational shear interferometer (RSI). The MSI, first implemented in 1878,[16] is the prototypical astrometry instrument and was used by Rosen and Yariv to demonstrate 3D coherence imaging. MSI has general utility as an interferometer, but because it collects only one correlation for each instrument position it is extraordinarily inefficient as an imaging instrument. The RSI has a much briefer history but still has been under investigation for more than three decades.[17] Roddier[2] and Roddier and Rodier[18] have used the RSI for 2D imaging, and Itoh et al.[19-22] used RSI data to reconstruct 3D data sets consisting of two spatial dimensions and one spectral dimension. The advantage of the RSI is that it samples entire planes of independent coherence measurements in parallel. In this section we briefly review data acquisition with the MSI and RSI, and we analyze the band volume and the impulse response for typical implementations of each instrument.

The MSI consists of two field-sampling ports mounted upon a single mechanical beam. One combines the field drawn from the sampling ports through an optical system to determine the mutual intensity between the two sampling points. Various mechanisms can be employed to adjust the relative path lengths from the sampling ports to the detector that determines the mutual intensity. The phase and the amplitude of the mutual intensity can be extracted from a spatial fringe pattern or by dithering of the relative delay of the optical paths. We do not consider the beam-combining optics here. It is useful, however, to consider the sample point geometry in the correlation plane, which is illustrated in Fig. 4. The sample points lie upon the mechanical beam that passes through the origin of the correlation plane. The beam rotates freely about the origin but cannot be displaced. The sample points may lie anywhere along the beam. We define the new variable r_{max} to be the maximum distance of a sampling point from the origin. r_{max} is also the radius of the correlation plane aperture and half of the length of the MSI beam.

We define three new variables to describe the state of the MSI. ϕ is the angle between the mechanical beam and the x axis. The range of ϕ is $[0, 2\pi]$. d is the separation between the sampling points. The range of d is $[0, 2r_{max}]$. $\hat{d}$ is the distance of the midpoint between the sampling ports from the origin. The range of $\hat{d}$ is $[(d/2) - r_{max}, r_{max} - (d/2)]$. The
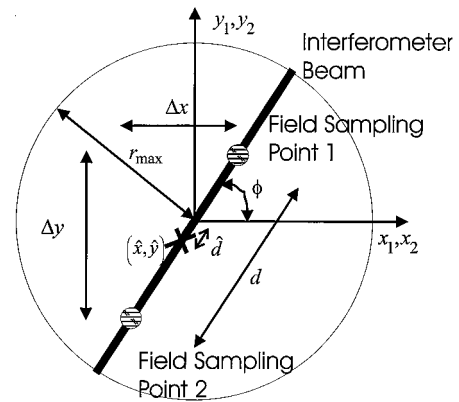

Fig. 4. Geometry of the MSI correlation plane: r_{max}, radius of the system aperture; d, sampling-point separation; $\hat{d}$, distance between the midpoint of the sampling points and the origin; ϕ, angle between the interferometer beam and the x axis.

sample space coordinates for a given interferometer state are

$$\Delta x = d \cos\phi,$$
$$\Delta y = d \sin\phi,$$
$$q = \hat{d}d. \qquad (15)$$

Using the ranges described above, we find that Δx and Δy cover the range $[-2r_{max}, 2r_{max}]$. The range of q varies as a function of Δx and Δy. For a given value of $d = \sqrt{\Delta x^2 + \Delta y^2}$, the range of q is $\{-d[r_{max} - (d/2)], d[r_{max} - (d/2)]\}$. The band volume is the range of $\mathbf{u}$ over which $\breve{I}(\mathbf{u})$ or $\breve{I}_p(\mathbf{u})$ can be sampled. The band volume is the Fourier transform of the impulse response $P_\rho(\mathbf{r}_s)$, which is used in Eqs. (6) and (14). In the far-field reconstruction of Eq. (5), we find that $\mathbf{u} = [(\Delta x/\lambda_0 R), (\Delta y/\lambda_0 R), (q/\lambda_0 R^2)]$. For the projective coordinates used in the Fresnel case, we find from Eq. (13) that $\mathbf{u} = [(\Delta x/\lambda_0), (\Delta y/\lambda_0), (q/\lambda_0)]$. In both cases the band volume is proportional to the range of $(\Delta x, \Delta y, q)$.

The band volume for the MSI is sketched in Fig. 5. The axes in the figure are scaled in terms of r_{max}/R, where R is the nominal distance from the source to the correlation plane. Because $r_{max}/R < 1$ in both the Fraunhofer and the Fresnel domains and because u_z scales as r_{max}^2/R^2, the u_z axis is greatly expanded relative to the u_x and u_y axes in the figure. The band volume is useful in estimating the resolution of source reconstruction and in designing the coherence sampling scheme. The resolution along any given direction can be approximated by the inverse of the extent of the band volume along that direction. This approximation yields transverse resolution $\lambda_0 R/r_{max}$ and longitudinal resolution $\lambda_0 R^2/r^2_{max}$ in the Fraunhofer zone. In the primed Fresnel-zone coordinates, the transverse resolution is λ_0/r_{max} and the longitudinal resolution is λ_0/r_{max}^2. Note that the transverse and the longitudinal coordinates are not in the same units. When the conversion factors from distorted to Cartesian space listed in Eq. (9) are applied, the Fresnel-zone resolution is also $\lambda_0 R/r_{max}$ in trans-
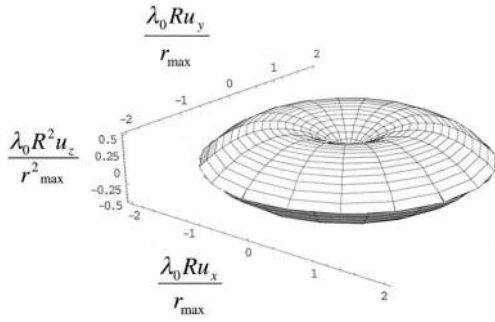
Fig. 5. Band volume for MSI sampling. The band volume is plotted in the real-space Fourier space of the source density for the Fraunhofer zone and in the projective-space Fourier space for the Fresnel zone. The coordinate axes correspond to the Fourier coordinates (u_x, u_y, u_z). The transverse coordinates are normalized with respect to $r_{max}/\lambda_0 R$. The longitudinal coordinate is normalized with respect to $r_{max}^2/\lambda_0 R^2$. Because $r_{max}/R \ll 1$, the normalization frequency for the longitudinal axis is less than it is for the transverse axes. The missing cone in the Fourier space along the u_z axis is characteristic of limited-angle tomographic systems.

verse coordinates and $\lambda_0 R^2/r_{max}^2$ longitudinally. These estimates are confirmed in models of the impulse response presented below.

The contraction of the band volume along the longitudinal axis near the origin (the "missing cone"[15]) acts as a high-pass filter on the reconstructed source distribution. This filtering has two effects: First, objects with high-frequency transverse spatial features will be better resolved longitudinally than more nearly uniform objects and, second, interference sampled between distant points covers more of the band volume and thus contains more information than interference between near neighbors. The first effect means that one could not resolve a longitudinally distributed set of uniform planar sources at all but that one could easily resolve discrete point sources. The Fourier-space representation of the planar sources is a set of points on the u_z axis, exactly orthogonal to the band volume. The Fourier representation of the point sources covers the u_x–u_y plane, fully overlapping the band volume. In view of the second point one may seek to measure correlation samples with separations that match the direction of the lobes of the band volume so that high-frequency details that provide depth information are not missed.

As was mentioned above, the MSI samples only one correlation per instrument position. Other designs based on RSI's are attractive because they sample complete planes in $(\Delta x, \Delta y)$ space in parallel. The primary components of the RSI, as illustrated in Fig. 6, are a beam splitter and two folding mirrors. The field incident upon the folding mirrors is reflected back through the output port of the beam splitter and detected at every point in the output plane. The folding mirrors consist of two planar reflectors joined at right angles. The folding mirrors are often implemented by the use of roof prisms. Each folding mirror inverts the reflected field about its fold axis. The
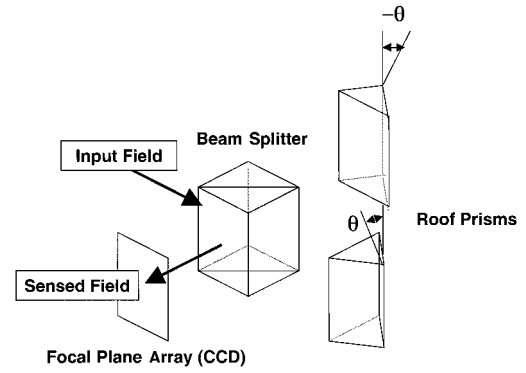

Fig. 6. Basic structure of a rotational shear interferometer. The RSI is a Michelson interferometer in which the plane retroreflection mirrors have been replaced with folding mirrors. The folding axes of the mirrors lie in the transverse plane at angles ϕ and $-\phi$ with respect to the x axis. The output port interferes differentially rotated wave fronts from the two mirrors.

fold axes of both mirrors lie in the transverse plane. As shown in Fig. 6, the fold axis of one mirror makes an angle θ with respect to the x axis. The fold axis of the other mirror makes an angle $-\theta$ with respect to the x axis. Let the transverse coordinates in the output planes of the RSI be (x_f, y_f). The field produced at the output point (x_f, y_f) by the fold mirror with an axis at angle θ relative to the x axis is the field that would appear at $(x_f \cos 2\theta - y_f \sin 2\theta, -x_f \sin 2\theta - y_f \cos 2\theta)$ if the fold mirror were replaced with a plane mirror. If, for example, $\theta = 0$, the fold mirror would reflect across the x axis and the output point (x_f, y_f) would correspond to the plane-mirror output point $(x_f, -y_f)$. The field produced at (x_f, y_f) by the $-\theta$ mirror would appear at $(x_f \cos 2\theta + y_f \sin 2\theta, x_f \sin 2\theta - y_f \cos 2\theta)$ if that mirror were replaced with a plane mirror. The mutual coherence between fields that is due to the two mirrors can be determined by longitudinal dithering of one of the fold mirrors. Each point in the output window samples the mutual coherence for a distinct transverse separation relative to the plane-mirror Michelson interferometer. The separations and mean positions for the mutual coherence sampled at (x_f, y_f) are

$$\Delta x(x_f, y_f) = 2y_f \sin(2\theta),$$
$$\Delta y(x_f, y_f) = 2x_f \sin(2\theta), \qquad (16)$$

$$\hat{x}(x_f, y_f, x_g) = 2x_f \cos(2\theta) + x_g,$$
$$\hat{y}(x_f, y_f, y_g) = -2y_f \cos(2\theta) + y_g, \qquad (17)$$

where (x_g, y_g) is the transverse displacement between the origins of the output plane coordinates and the source volume coordinates. The q coordinate at each point in the output plane is

$$q = \Delta x(x_f, y_f)\hat{x}(x_f, y_f, x_g) + \Delta y(x_f, y_f)\hat{y}(x_f, y_f, x_g)$$
$$= (y_f x_g - x_f y_g)\sin(2\theta). \qquad (18)$$

A RSI samples a surface in $(\Delta x, \Delta y, q)$ space for each value for (x_g, y_g). To sample the entire accessible 3D
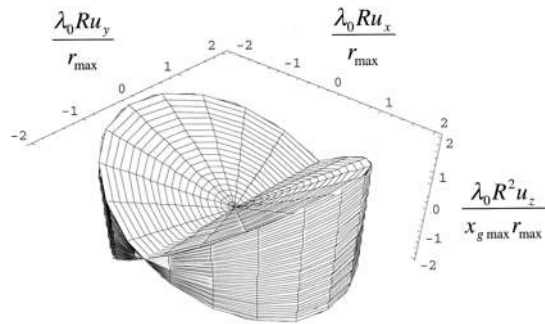
Fig. 7. Band volume for linear translation RSI sampling. The situation is identical to that of Fig. 4, except that the normalization of the u_z axis is now $x_{g_{max}} r_{max} / \lambda_0 R^2$. $x_{g_{max}}$ is the linear displacement range for the RSI. For the RSI of this figure, $\phi = \pi/4$ and the fold axes of the two mirrors are perpendicular. In this geometry, the RSI is also called a wave-front folding interferometer.

$(\Delta x, \Delta y, q)$ space one translates the interferometer in (x_g, y_g).

As for the MSI, let r_{max} be the radius of the RSI aperture. Let $x_{g_{max}}$ be the distance over which the RSI is translated transversely to the optical axis. The band volume captured by a RSI with $\theta = \pi/4$ translated linearly along the x_g axis is shown in Fig. 7. $\theta = \pi/4$ corresponds to a special class of RSI, the wave-front folding interferometer.[23] The crease in the band volume of Fig. 7 along the u_y axis is due to the fact that q vanishes normally to the translation direction for linear translation of the RSI so that only object features and edges perpendicular to the path contribute to longitudinal resolution. This crease can be avoided by translation of the RSI along a nonlinear path. For example, Fig. 8 shows the band volume when RSI with circular aperture r_{max} is translated in a circle of radius $x_{g_{max}}$. Reducing θ decreases the effective aperture of the RSI and thereby decreases its resolution. This may be desirable, particularly if one wishes to match interference fringes in the output plane to a CCD pixel spacing.

We now consider impulse responses for MSI and RSI systems. As a benchmark of the resolution of these systems, we calculate impulse response under
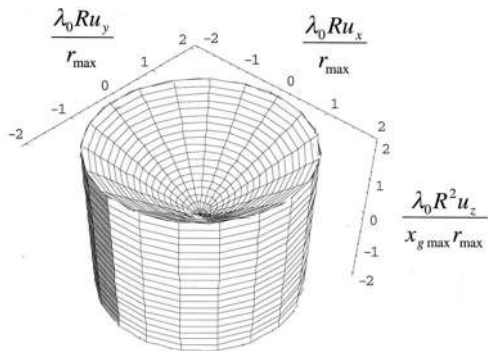

Fig. 8. Band volume for imaging with a circularly translated RSI. The situation is identical to that of Fig. 6, except that $x_{g_{max}}$ now represents the radius of the circle about which the optical axis of the RSI is translated.
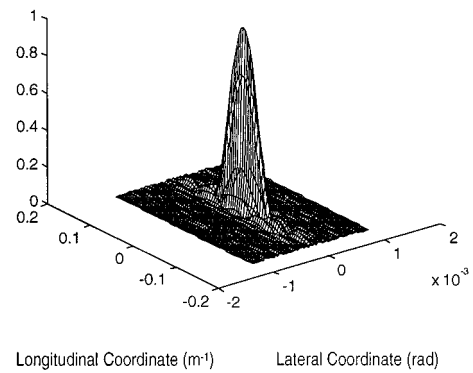

Longitudinal Coordinate (m⁻¹)   Lateral Coordinate (rad)

Fig. 9. Surface plot of the 3D MSI impulse response in the x'–z' plane. The vertical axis is normalized to the maximum response. The spatial axes are in projective coordinates, with units of inverse meters for the longitudinal axis and radians for the transverse axis. The impulse response is approximately shift invariant in the projective space; it is not shift invariant in real space. To obtain the real-space impulse response one adds $1/R$ to the longitudinal range and takes the inverse. For an impulse at 1 m, a point at $z' = 0.1$ is at $z = 1/(1 + 0.1) = 0.91$. A point at $z' = -0.1$ is at $z = 1/(1 - 0.1) = 1.11$.

the assumption that the correlation plane aperture is fixed in space. This assumption is not likely to reflect practical RSI uses in which the aperture moves with the instrument, but a fixed aperture gives us a common basis for comparing the two interferometers. To find the impulse response for the fixed aperture we set correlations between pairs of points where either pair of correlated points (x_1, y_1) or (x_2, y_2) was outside the aperture $(x_1^2 + y_1^2) > r_{max}^2)$ or $(x_2^2 + y_2^2) > r_{max}^2)$ to zero.

We model the impulse response of a Fresnel-zone imaging system by calculating the mutual intensity as a function of space, using Eq. (13), and then inverting the mutual intensity to find the filtered source intensity, using Eq. (14), under aperture and sampling constraints of the imaging system. Our simulations use a discrete $64 \times 64 \times 64$ point-source volume, consisting of one nonzero intensity point, that was propagated by means of a fast Fourier transform to provide the mutual intensity correlations as a function of Δx, Δy, and q. We then inverse by fast Fourier transform the mutual intensity to reconstruct the filtered source intensity. Because the input is a single point, this reconstruction is the impulse response. In general, each $(\Delta x, \Delta y, q)$ corresponds to multiple pairs of correlation plane points (x_1, y_1) or (x_2, y_2). The MSI and RSI approaches, as well as other potential sampling schemes, improve sampling efficiency by associating each $(\Delta x, \Delta y, q)$ with unique values of (x_1, y_1) and (x_2, y_2).

Figure 9 is a surface plot of a cross section of the impulse response for MSI sampling for a 0.5-cm aperture and a wavelength of 632.8 nm. The lateral coordinate is in angular units and the longitudinal coordinate is in units of inverse distance, consistent with the primed coordinate system. To transform these units into real space, one multiplies the transverse coordinate by the source–correlation plane dis-
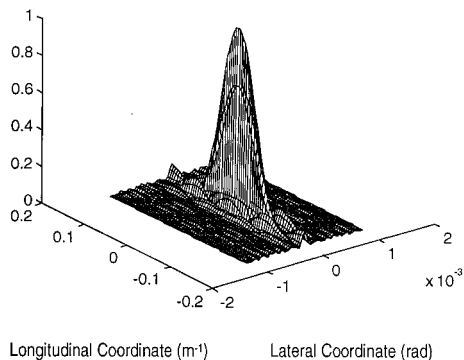
Fig. 10. Cross section of the RSI impulse response in the x'–z' plane under the same constraints as for Fig. 9.

tance and the longitudinal coordinate by the square of this distance. At 2 m, for example, the center spot size is approximately 0.025 cm along the transverse axis and 14 cm along the longitudinal axis. Figure 10 is the cross section of the RSI impulse response. The values of all sampling parameters were identical for both simulations.

To compare the resolution of the two sampling schemes we use relations between lateral and longitudinal resolution and aperture size:

$$x'_{\text{res}} = \frac{C_x \lambda}{d}, \qquad z'_{\text{res}} = \frac{C_z \lambda}{d^2}, \qquad (19)$$

where x'_{res} is the lateral resolution size in radians, z'_{res} is the longitudinal resolution size in inverse length, d is the aperture diameter, and C_x and C_z are sampling-scheme-dependent unitless constants, where a smaller number indicates a smaller resolution element size or better resolution. The resolution here is not calculated with the Rayleigh two-point criterion; rather, it uses the root-mean-square size of the point-spread function (PSF). For the MSI, $C_x = 0.95$ and $C_z = 1.38$, whereas for the RSI, $C_x = 1.15$ and $C_z = 1.65$.

Under the definition of aperture used here, there is little difference in resolution between the RSI and the MSI sampling schemes. Each of the sampling schemes has its own advantages and disadvantages, however. The MSI scheme most effectively utilizes a circular aperture of a given size because the translation $(\hat{x}, \hat{y})$ is always in the same direction as the displacement $(\Delta x, \Delta y)$, so the value of q is maximized. The MSI approach will contain more correlations within a fixed sized aperture and therefore is expected to provide superior longitudinal resolution. Our simulations seem to indicate that this difference may not be great because the two methods yield similar impulse responses. The advantages of the RSI approach are that data are taken in parallel and that the higher acquisition speed makes translation of the instrument more attractive. Parallel acquisition speeds acquisition and reduces stabilization requirements. By translating the instrument as a whole one avoids the fixed-aperture assumption of our simulations, to permit a greater range for the mean

transverse displacement of sample points than for the maximum sample separation. This approach can substantially improve the resolution obtained.

4. Experimental Results

We explored our PSF models experimentally by measuring correlations produced by a laser diode with a RSI. We measured the correlations by translating the RSI laterally perpendicular to the RSI optical axis and sampling the interference intensity with various phase shifts at each lateral position.

Our RSI consisted of a 5.08-cm-aperture cube beam splitter with two 5.08-cm folding mirrors, each constructed from two separate mirrors affixed to each other at a 90-deg angle (Fig. 11). Each of the mirrors could be independently rotated about its axis such that the shear angle and the alignment axis could be set. The focal-plane array was a Princeton Instruments 512×512 backilluminated CCD camera placed at the output face of the RSI. To provide the longitudinal delay, one of the folding mirrors was placed upon a piezo-driven flexure stage, which permitted precise control of relative path length down to 10-nm resolution when it was used in conjunction with an inductive positioning sensor. All these optical components were in suitable optical mounts and bolted to a 1.9-cm-thick stainless-steel plate, which was itself bolted to a 1.27-cm-thick steel plate to provide the required vibration stability to minimize noise. The bottom plate was placed upon two steel rails, and the RSI was moved along the rails by an Aerotech translation stage, which could move the interferometer over a 5-cm distance. Even with the extremely rigid steel, the plates collectively bent enough to change the path length delay ~20 μm over its full range of travel, and this misadjustment was repeatable and corrected for when the path-length delay was set.

We measured the impulse response of this system by using a laser diode that had a center wavelength of 660 nm. The diode facets were damaged to inhibit lasing, and the device was used as a LED with a 20-nm spectral bandwidth. The source provided an elliptical radiation pattern that completely filled the aperture. An iris was used as the pupil stop to control the aperture size. The RSI imaged the source at 256 different positions of the translation stage separated by 34 μm. At each transverse RSI position, images were recorded for eight different relative path delays between the folding mirrors. These longitudinal dithers were separated by 0.125 wavelength, centered about zero path delay. The complex mutual intensity across the RSI output plane was isolated from these eight measurements in two steps. First we multiplied the 2D pattern recorded for each delay by the phase factor $\exp(-j4\pi\delta/\lambda_0)$, where δ is the path delay. Then we summed all eight modulated frames. This process isolates the component of the output intensity that oscillates at the frequency $2/\lambda_0$ under longitudinal dithering. This component is the mutual intensity. The RSI detects the mutual intensity as a function of Δx and Δy on the Cartesian
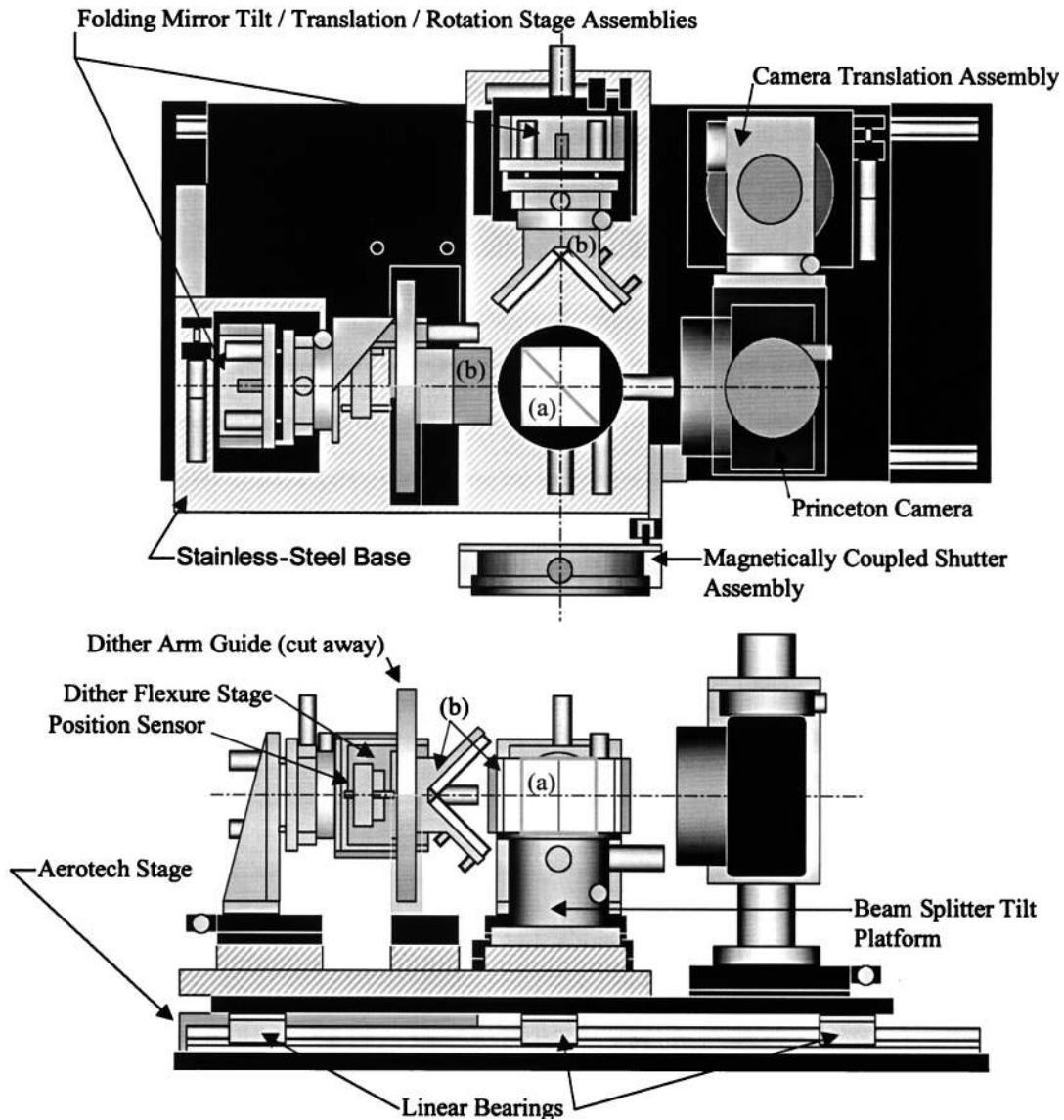
Fig. 11. RSI used to measure the mutual coherence of the four-LED test object and RSI impulse response. The RSI consisted of (a) a 5 cm × 5 cm × 5 cm cube beam splitter with (b) two 5 cm × 5 cm folding mirrors. Each folding mirror was constructed from two separate mirrors affixed to each other at a 90-deg angle, giving a full 5 cm × 5 cm square aperture. A Princeton Instruments 512 × 512 backilluminated CCD was used as the focal-plane array. For longitudinal delay, one of the folding mirrors was placed upon a piezoelectric-driven flexure stage in conjunction with an inductive positioning sensor. The RSI was mounted upon two linear bearings and was translated over a 5-cm length by an Aerotech translation stage.

CCD grid and for uniform shifts in x_g. We transformed these measurements into uniform estimates of $J_{3D}(n\Delta x, m\Delta y, l\hat{x}\Delta x)$ for integrals n, m, and l by a series of one-dimensional interpolations. We used the approximate prolate-spheroidal interpolation series[24] to implement this transformation. We then implemented a 3D fast Fourier transform of $J_{3D}(n\Delta x, m\Delta y, l\hat{x}\Delta x)$ over the indices n, l, and m to obtain the function $I(x/z, y/z, 1/z)/z^2$.

The lateral aperture diameter in our PSF experiment was 5.6 mm. The RSI was set with a 90-deg rotational shear angle, and the total translation distance was 8.7 mm to ensure full sampling of the aperture. The results of the 3D reconstructed PSF are shown in Fig. 12. Because the simulated and

measured aperture sizes were so similar, there is close agreement between the sizes of the measured and the simulated PSF's. There is a slight asymmetry in the measured PSF, because the iris is not completely coincident with the axis of the RSI at the center position of the lateral travel.

We also used this experimental system to reconstruct more-complex sources. For example, we imaged a source consisting of four light-emitting diodes at $\lambda_0 = 640$ nm. In this case, no aperture stop was used to limit resolution. The mutual intensity was measured by the RSI with its shear angle set to 19 deg. The RSI was translated laterally by a micrometer-resolution translation stage to 256 different positions 193 μm apart. We obtained a 2D measure of the
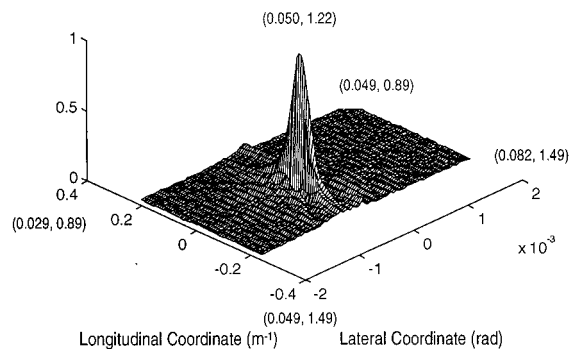
Fig. 12. Experimental cross section of the RSI impulse response in the $x'–z'$ plane. The four corners of the plane and the peak are labeled with their Cartesian coordinates in real space, in meters, relative to the origin of the focal-plane array. This impulse response was sampled by a linearly translated RSI by use of the procedure and the experimental parameters described in the text.
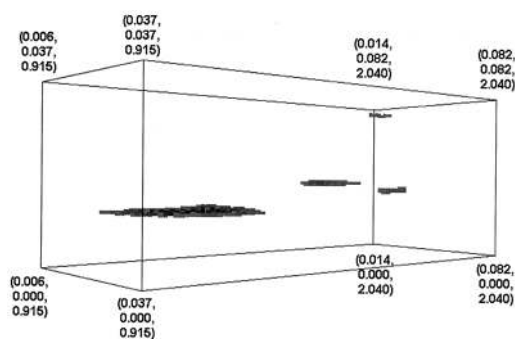

Fig. 13. Experimental reconstruction of a four-light-emitting-diode test source, as sampled by the RSI. The 50% power density isosurface is shown. The LED's appear to be of different sizes because they were in fact of different intensities. The source is shown in projective coordinates, but the corners are labeled in Cartesian coordinates, in meters, relative to the origin of the focal-plane array. These data were taken by a RSI by use of the procedure and the experimental parameters described in the text.

mutual intensity at each position, using the eight-longitudinal-position approach described above for the PSF measurement. Figure 13 shows the estimated power density of the LED sources as a 50% constant isosurface of the maximum power density in the source. Because the LED's provide differing intensities, each appears to be a different size, when they were in fact all similarly sized. Three of the LED's were in a rear plane approximately 1.5 m from the RSI pupil plane and one was 1 m away. The longitudinal accuracy of reconstruction was approximately 0.2 m^{-1}, or 20 cm at a 1-m distance. These results demonstrate that lensless imaging of 3D sources with coherence measurements alone is possible.

5. Conclusion

We have shown that finite-aperture 3D coherence imaging can be extended to the Fresnel diffraction zone by straightforward Fourier analysis, and we have analyzed the resolution of both Fraunhofer- and Fresnel-zone imaging. The PSF of a rotational shearing interferometer was also experimentally measured. Although coherence imaging holds the potential to revolutionize 3D imaging, several further questions remain to be addressed. Most notably, noise issues are not addressed here but will play an important role in computational coherence imaging. It is interesting to note that, in contrast with the point-to-point independence of conventional imaging systems, system noise scales with object complexity in coherence imaging systems. When the information capacity of a conventional imaging system is limited only by the space–bandwidth product, the information capacity of a coherence imaging system will be limited by both the space–band volume product and noise scaling.

References

1. C. V. Schooneveld, ed., *Image Formation from Coherence Functions in Astronomy*, Vol. 76 of International Astronomical Union Colloquium 49 (Reidel, Dordrecht, The Netherlands, 1978).
2. F. Roddier, "Interferometric imaging in optical astronomy," Phys. Rep. **170,** 97–166 (1988).
3. G. W. Swenson, "Radio astronomy precedent for optical interferometer imaging," J. Opt. Soc. Am. A **3,** 1311–1319 (1986).
4. J. T. Armstrong, D. J. Hutter, K. J. Johnston, and D. Mozurkewich, "Stellar optical interferometry in the 1990s," Phys. Today **48**(5), 42–49 (1995).
5. A. J. Devaney, "The inverse problem for random sources," J. Math. Phys. **20,** 1687–1691 (1979).
6. W. H. Carter and E. Wolf, "Correlation theory of wavefields generated by fluctuating, three-dimensional, primary, scalar sources. I. General theory," Opt. Acta **28,** 227–244 (1981).
7. I. J. LaHaie, "Inverse source problem for three-dimensional partially coherent sources and fields," J. Opt. Soc. Am. A **2,** 35–45 (1985).
8. A. M. Zarubin, "Three-dimensional generalization of the van Cittert–Zernike theorem to wave and particle scattering," Opt. Commun. **100,** 491–507 (1993).
9. J. Rosen and A. Yariv, "General theorem of spatial coherence: application to three-dimensional imaging," J. Opt. Soc. Am. **13,** 2091–2095 (1996).
10. J. Rosen and A. Yariv, "Reconstruction of longitudinal distributed incoherent sources," Opt. Lett. **21,** 1803–1806 (1996).
11. J. Rosen and A. Yariv, "Three-dimensional imaging of random radiation sources," Opt. Lett. **21,** 1011–1014 (1996).
12. B. R. Frieden, "Optical transfer of the three-dimensional object," J. Opt. Soc. Am. **57,** 56–66 (1967).
13. A. W. Lohmann, "Three-dimensional properties of wavefields," Optik **51,** 105–117 (1978).
14. L. Mandel and E. Wolf, *Optical Coherence and Quantum Optics* (Cambridge U. Press, Cambridge, 1995).
15. M. Y. Chiu, H. H. Barrett, R. G. Simpson, C. Chou, J. W. Ardent, and G. R. Gindi, "Three-dimensional radiographic imaging with a restricted view angle," J. Opt. Soc. Am. **69,** 1323–1333 (1979).

16. D. H. DeVorkin, "Michelson and the problem of stellar diameters," J. Hist. Astron. **6,** 1–18 (1975).
17. J. D. Armitage and A. Lohmann, "Rotary shearing interferometry," Opt. Acta **12,** 185–192 (1965).
18. C. Roddier and F. Roddier, "Imaging with a coherence interferometer in optical astronomy," in *Image Formation from Coherence Functions in Astronomy*, C. V. Schooneveld, ed., Vol. 76 of International Astronomical Union Colloquium 49 (Reidel, Dordrecht, The Netherlands, 1979), pp. 175–179.
19. K. Itoh and Y. Ohtsuka, "Fourier-transform spectral imaging: retrieval of source information from three-dimensional spatial coherence," J. Opt. Soc. Am. A **3,** 94–100 (1986).
20. K. Itoh, T. Inoue, T. Yoshida, and Y. Ichioka, "Interferometric supermultispectral imaging," Appl. Opt. **29,** 1625–1630 (1990).
21. K. Itoh, T. Inoue, and Y. Ichioka, "Interferometric spectral imaging and optical three-dimensional Fourier transformation," J. J. Appl. Phys. **29,** L1561–L1564 (1990).
22. K. Itoh, "Interferometric multispectral imaging," in *Progress in Optics*, E. Wolf, ed. (North-Holland, Amsterdam, 1996), Vol. 35, pp. 145–196.
23. L. Mertz, *Transformations in Optics* (Wiley, New York, 1965).
24. J. J. Knab, "Interpolation of band-limited functions using the approximate prolate series," IEEE Trans. Inf. Theory **IT-25**, 717–720 (1979).